International Journal of Solids and Structures 122–123 (2017) 196–209

Contents lists available at ScienceDirect

International Journal of Solids and Structures

journal homepage: www.elsevier.com/locate/ijsolstr

Compression and recovery of carbon nanotube forests described as a phase transition

Xiaojun Liang[a], Jungho Shin[b], Daniel Magagnosc[b], Yijie Jiang[a], Sei Jin Park[c], A. John Hart[c], Kevin Turner[a], Daniel S. Gianola[b,d], Prashant K. Purohit[a,*]

[a] Department of Mechanical Engineering and Applied Mechanics, University of Pennsylvania, Philadelphia, PA 19104, USA
[b] Department of Materials Science and Engineering, University of Pennsylvania, Philadelphia, PA 19104, USA
[c] Department of Mechanical Engineering, Massachusetts Institute of Technology, Cambridge, MA 02139, USA
[d] Department of Materials, University of California Santa Barbara, Santa Barbara, CA 93106, USA

ARTICLE INFO

Article history:
Received 28 November 2016
Revised 16 May 2017
Available online 20 June 2017

Keywords:
Nanoindentation
CNT foams
Phase transition

ABSTRACT

In this paper we describe experiments and a continuum phase transition model for the compression of carbon nanotube (CNT) forests. Our model is inspired by the observation of one or more moving interfaces across which densified and rarefied phases of the CNT forests co-exist. We use a quasi-static version of the Abeyaratne-Knowles theory of phase transitions for continua with a stick-slip type kinetic law and a nucleation criterion based on the critical stress for buckling of CNT forests to describe the formation and motion of these interfaces in uniaxial compression experiments. We investigate micropillars made from bare CNTs, as well as those coated with different thicknesses of alumina using atomic layer deposition (ALD). The coating thickness affects the moduli of individual CNTs as well as the adhesion energy per contact between CNTs. In order to test the applicability of our model to more complex stress states, we carry out nanoindentation experiments on the CNT pillars and interpret the load-indentation data by incorporating a constitutive law allowing for phase transitions into solutions for the indentation of a linearly elastic half-space. Even though the state of stress in a nanoindentation experiment is more complex than that in a uniaxial compression test, we find that the parameters extracted from the nanoindentation experiments are close to those from uniaxial compression. Our models could therefore aid the design of CNT forests to have engineered mechanical properties, and guide further understanding of their behavior under large deformations.

1. Introduction

Carbon nanotubes (CNTs) are well known to have high elastic modulus Treacy et al. (1996) and strength Peng et al. (2008), along with excellent electrical and thermal conductivity Li et al. (2005); Yu et al. (2005). When synthesized at high density on a substrate, it is typical for the CNTs to self-organize such that they are nominally vertically aligned Bedewy et al. (2012), sometimes called carpets or forests, wherein the CNTs are wavy yet have a general orientation perpendicular to the substrate (see Fig. 1) Fan et al. (1999); Hata et al. (2004). This efficient means of organizing the CNTs into anisotropic films having thickness ranging from the micrometer to multi-millimeter scale, has spurred wide studies of their potential use as, for example, thermal and electrical interfaces Taphouse et al. (2014); Tawfick et al. (2009), composite materials Coleman et al. (2006); Meaud et al. (2014); BrielandShoultz et al. (2014), and filtration membranes Halonen et al. (2010). In all cases, the properties of the CNT forest are intimately related to the dimensions, density, and orientation of the CNTs, which may also vary spatially through the forest Bedewy et al. (2011); Park et al. (2013a). CNTs can be reasonably described as slender beams, therefore it is well accepted that the CNT forest can be considered as a fiber network or foam Cao et al. (2005); Zbib et al. (2008); Hutchens et al. (2010); 2011). However, the complex mechanical behavior observed upon compression of CNT forests, and its general relation to the attributes of CNT diameter, density, and orientation, is not yet well understood.

Although ideas from the mechanics of fiber networks have not yet been applied to CNT forests, the compressive behavior of fiber networks has been studied in other contexts. For example, the mechanics of yarns, such as wool, was examined in the textile literature many decades ago and it was recognized that compression of this type of fibrous masses was dominated by the bending and

* Corresponding author.
E-mail address: purohit@seas.upenn.edu (P.K. Purohit).

http://dx.doi.org/10.1016/j.ijsolstr.2017.06.025
0020-7683/

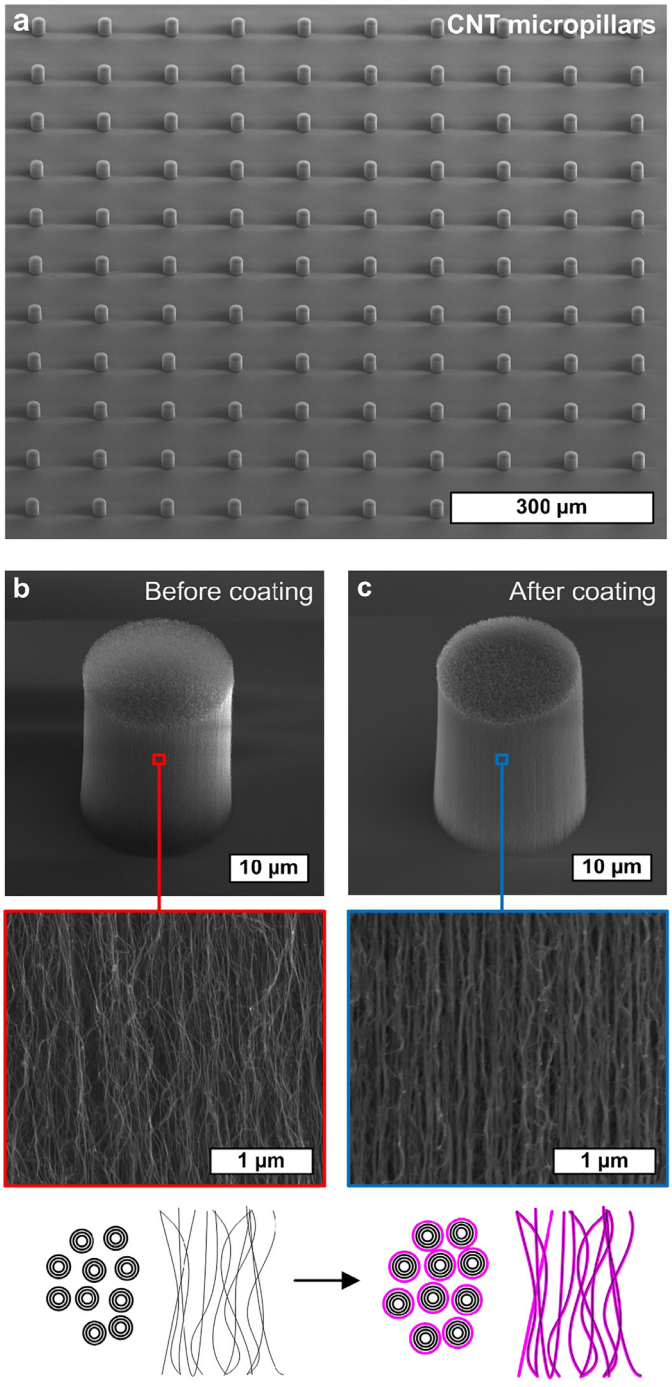

Fig. 1. (a) SEM image of an array of CNT pillars used for mechanical characterization; (b) SEM image of individual pillar, close-up of CNT forests as viewed from sidewall, and top/side view schematic of CNT forests without ALD coating; (c) corresponding images after ALD coating with Al_2O_3.

buckling of fibers. Pursuing this idea, Van Wyk (1946) determined a relation between the Cauchy stress and fiber volume fraction in the current configuration in terms of the network parameters and bending modulus of the fibers. Subsequent work applied similar ideas to many other fiber networks, such as, glass wool, paper, etc., and confirmed that Van Wyk's relation describes the compressive behavior quite well Toll (1998). Recent modifications to the theory include accounting for steric hindrances Komori and Itoh (1994), friction between fibers Barbier et al. (2009), and fiber crimp Lee et al. (1992). A vast literature also exists for the tensile and shear behavior of fiber networks that we do not describe here for the sake of brevity, but is well described in a review article Onck et al. (2005).

The compression behavior of fiber networks is similar to that of foams Onck et al. (2005). In particular, it has been demonstrated that buckling of fibers during compression often happens in a localized manner so that one or more moving interfaces separate a densified region of the network (or foam) from a rarefied region. A few papers have described the motion of these interfaces using a theory of phase transitions by recognizing that in both dynamic and quasi-static experiments the rarefied and densified regions of the network (or foam) can coexist over a range of stresses Gong et al. (2005); Kim et al. (2015); Lakes et al. (1993). In this paper we apply a phase transitions based model to the compression response of vertically aligned CNT forests, obtained via quantitative *in situ* micro-compression experiments. We assume that the CNT forest is an elastic foam with a stored energy function that has two wells (or minima) – one corresponding to the rarefied phase in which the CNTs are mostly straight, and the other corresponding to the densified phase in which the CNTs are mostly buckled with a large number of contacts between them. The existence of broad convex regions around the minima in the energy landscape of CNT forests is attributed in Qiu et al. (2011) to the reversibility of the deformation under moderate strains (as seen in experiments Qiu et al. (2011); McCarter et al. (2006) as well as simulations Radhakrishnan et al. (2013)). Such reversibility is also characteristic of phase changing materials whose Helmholtz free energy function has multiple minima, each of which correspond to different micro-structure Bhattacharya (2003); Abeyaratne and Knowles (2006). In order to accommodate the deformations imposed on the boundary, a phase changing material forms microstructure in the bulk in which different phases co-exist at the same stress Bhattacharya (2003); Abeyaratne and Knowles (2006); analogously, there is a range of stresses at which the densified and rarefied phases of CNT forests can co-exist to accommodate deformations imposed at the boundary. The idea of a multi-well energy landscape has appeared in a series of papers that describe the CNT forests as a one-dimensional mass-spring chain in which the springs are characterized by a double well potential Fraternali et al. (2011); Blesgen et al. (2012); Raney et al. (2013a); 2013b); Thevamaran et al. (2015). These models acknowledge the multiscale nature of the mechanical response of CNT forests and allow for the possibility that the properties could be graded Blesgen et al. (2012), so that the buckling load of the fibers could be a function of position. They also predict discrete jumps in the load-displacement curves (as the springs jump from one energy minimum to another) much like the discrete buckling events of CNT forests loaded in uniaxial compression. A continuum limit of this type of model has also been obtained and used to interpret the dissipation in loading/unloading experiments Raney et al. (2013a). However, these models do not connect the micro-structural parameters of the CNT forests (such as, density, CNT diameter) with the constitutive parameters entering the model as is done in the literature on foams. A micro-structural connection based on the mechanics of foams has been presented by Hutchens et al. (2012) who recognize that CNTs can adhere to each other causing a reduction in the energy of the forest under compression (see also Zbib et al. (2008)). Hutchens et al. connect the microscopic sticking behavior of CNTs to a visco-plastic hardening rule used in a fully three-dimensional computational framework Hutchens et al. (2011). A more comprehensive nano-scale computational model which represents CNTs in a forest as elastica finite elements with van der Waals interactions was described by Torabi et al. (2014) and Volkov et al. (2009). Torabi et al. (2014) establish relationships between post-buckling stress, initial elastic modulus, and buckling wavelength on statistical parameters (tortuosity, density and connectiv-

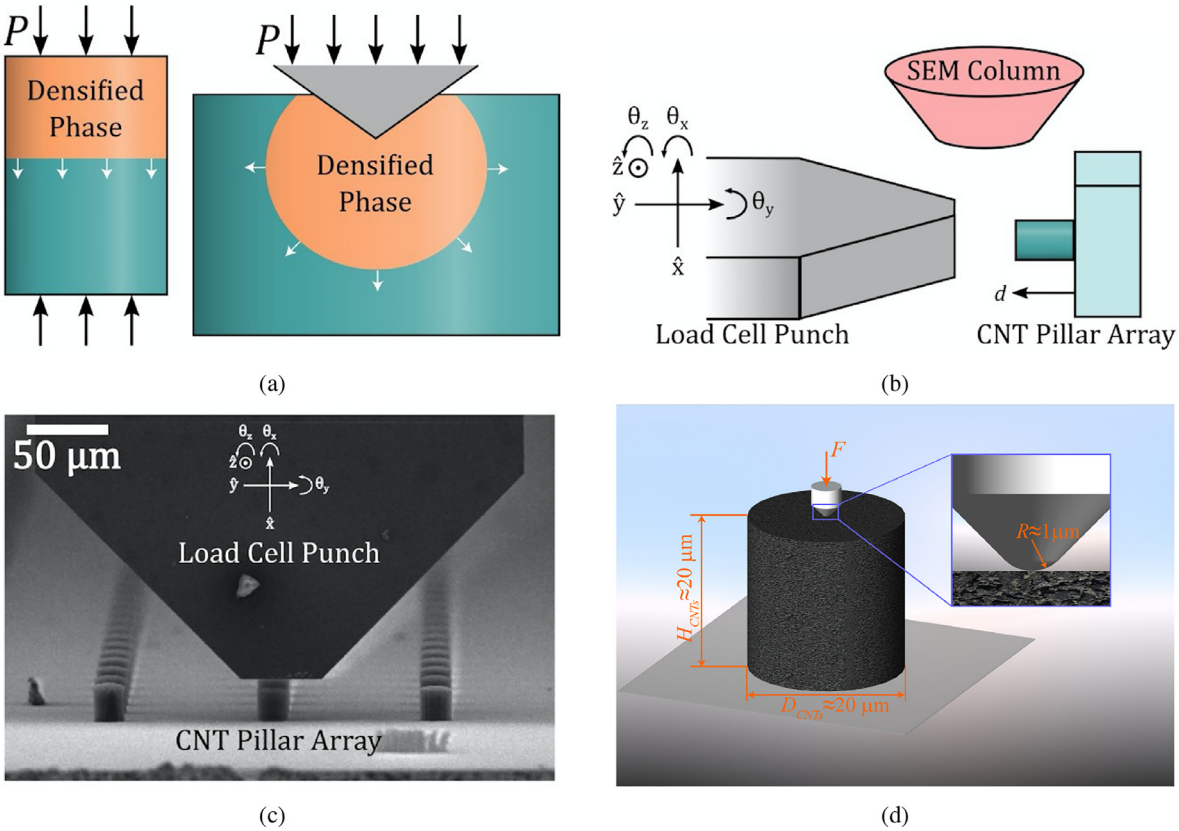

Fig. 2. (a) Schematic of two experimental configurations (and, thus, stress states) investigated: uniaxial pillar compression (left) and nanoindentation (right). In each case an interface, or phase boundary, separates the densified and rarefied phases. The phase boundary is flat in the uniaxial compression experiments and has an axi-symmetric shape in the nanoindentation experiments. As the load P increases, the volume of the densified phase increases by the outward motion of the phase boundary (shown by arrows). (b) Schematic of *in situ* SEM mechanical testing configuration used for pillar compression, and (c) low-magnification SEM image of testing apparatus and pillar specimens. (d) Illustration of nanoindentation test on a CNT pillar.

ity) of a CNT forest which a macroscopic constitutive model, ideally, should reproduce. Separately, it has been argued that such a macroscopic constitutive law for describing coordinated buckling of CNT forests should be *local* because constitutive properties exhibit only statistical variations across a CNT forest from top to bottom as demonstrated by uniaxial compression and nanoindentation experiments of Qiu et al. (2011).

Here we use a local *continuum* phase transition theory to study the uniaxial compression of CNT forests and include phase boundary kinetics as well as a nucleation criterion to describe features seen in the stress-strain curves. In contrast to a discrete mass-spring chain, a continuum phase transition model describes layer buckling of CNT forests as continuous interface (separating rarefied and densified phases) propagation (see cartoon in Fig. 2a). We (and others) have shown in recent work that the dynamics of discrete bi-stable mass-spring chains can be captured by a continuum phase transition theory if information lost in going from the discrete to continuum description is distilled into a kinetic relation and nucleation criterion that are supplied as constitutive information to the continuum theory Zhao and Purohit (2016); Zhao et al. (2015); Truskinovsky and Vainchtein (2005). A continuum phase transitions model, in contrast to a discrete mass-spring chain, is needed to model the response of CNT forests under loading configurations that are more complex than uniaxial compression. Here we demonstrate this idea by using our constitutive model to interpret indentation experiments on the CNT forests in which the stress and strain fields are inherently three-dimensional (see Fig. 2a). Phenomenological constitutive models that capture the load-indentation depth curves in nanoindentation experiments have been implemented recently using finite elements by Radhakrishnan et al. (2013), but to the best of our knowledge, these models have not been used to explain the collective buckling of CNT forests under uniaxial compression. In contrast, our continuum model can be applied to both uniaxial compression as well as nanoindentation experiments. It is characterized by a double-well energy landscape, much like the springs of Fraternali et al. (2011) and Blesgen et al. (2012), but it incorporates a rate-dependent kinetic law to describe the motion of phase boundaries in the spirit of Hutchens et al. (2011). Hutchens et al. (2011) used a visco-plastic computational model because the deformation of the CNT forests in their experiments was not fully recoverable. In contrast, the CNT forests in our experiments showed deformations that were largely recoverable with hysteresis, similar to Cao et al. (2005); Pathak et al. (2012).

The paper is organized as follows. In Section 2 we describe the preparation of the CNT forest samples. In Section 3 we describe the *in situ* scanning electron microscopy (SEM) experiments, and how the data from the compression experiments is interpreted using a phase transitions model. An insight that is confirmed by our analysis of the experimental data within a phase transitions model is that in agreement with the work of Torabi et al. (2014) the buckling wavelength varies inversely as the buckling load of the CNT forests and may be related to the energy of the interface separating the rarefied and densified phases. In Section 4 we briefly describe the nanoindentation experiments on the same samples, and how the data from these experiments can be interpreted by incorporating a linearized version of our phase transitions based model into solutions for indentation of an elastic half-space. The purpose of

Section 4 is to show that our continuum phase transitions model from Section 3 can predict the response of the CNT forests to indentation even though the state of stress in indentation is very different from that in uniaxial compression. We close with the main conclusions in Section 5.

2. Preparation of CNT pillars

2.1. CNT forest growth

For the growth of vertically aligned CNTs (see Fig. 1), an Al_2O_3/Fe catalyst layer is first patterned on4″ (100) silicon wafers coated with 300 nm of thermally grown SiO_2, by lift-off processing using photo-lithography followed by ultrasonic agitation in acetone. The supported catalyst layer, 10 nm of Al_2O_3 and 1 nm of Fe, is sequentially deposited by electron beam physical vapor deposition. The wafer with the deposited catalyst is diced into 1 × 1 cm pieces, and for each sample one piece is placed in the quartz tube furnace for the CNT growth. The growth recipe starts with flowing 100/400 s.c.c.m. of He/H_2 while heating the furnace up to 775 °C over 10 min (ramping step); then the temperature is held at 775 °C for 10 min with the same gas flow rates (annealing step). Then the gas flow is changed to 100/400/100 s.c.c.m. of $C_2H_4/He/H_2$ at 775 °C for CNT growth for the selected duration based on the typical growth rate of approximately 100 μm/min (growth step). Once the desired growth time has passed, the same gas flow is maintained while the furnace is turned off, allowing the system to cool. Once the furnace temperature reaches below 100 °C, 1000 s.c.c.m. of He is maintained for 5 min to purge the quartz tube before the samples are retrieved.

2.2. ALD Al_2O_3 coating

For some samples, the as-grown CNT samples are then coated with Al_2O_3 via ALD (Arradiance, GEMStar XT); each cycle deposits 1.1-1.3 Å of Al_2O_3. Trimethylaluminum, $Al_2(CH_3)_6$, and ozone, O_3, were used as the precursors. The deposition is performed at 175 °C and 1 Torr, and between introduction of each precursor, the chamber is evacuated to ensure that no residual precursor remained in the chamber.

3. Compression of the CNT forests

3.1. Experiment

After CNT growth and ALD coating, the CNT forests patterned as pillar compression specimens are placed in a custom nanomechanical testing apparatus for quantitative *in situ* mechanical testing in a scanning electron microscope (SEM). The testing apparatus consists of three key components: a 6-DOF closed loop nanopositioning stage (SmarAct GmbH), a linear piezoelectric actuator (Physik Instrumente GmbH), and a MEMS-based silicon capacitive load cell (FemtoTools AG) as illustrated in Fig. 2b. The apparatus has been described in detail previously Magagnosc et al. (2013); Zhao et al. (2015). The testing setup is installed in a high resolution SEM (FEI Quanta) for mechanical testing of the CNT pillars and simultaneous high resolution observation (see Fig. 2c).

Testing was performed according to the following procedure. The SEM stage was tilted by $< 5°$ to provide an unobstructed view of the CNT pillar array as depicted in Fig. 2c. A coarse angular alignment of the load cell indenter to the CNT pillars was first performed visually. Fine angular alignment was achieved using the previously reported contact stiffness method Zhao et al. (2015) on the CNT growth substrate. By maximizing contact stiffness, good alignment of the CNT pillars and load cell was ensured, most notably in the y-z plane (out of the imaging plane). The load cell was then visually aligned in the x, y, and z directions with a selected pillar for testing. Quasi-displacement controlled uniaxial compression was performed while recording the actuator displacement, force, and an imaging sequence at nominal strain rates between 0.001 s^{-1} and 0.1 s^{-1}.

The pillars tested here generally showed different moduli and plateau stresses, yet consistent loading behavior regardless of ALD coating thickness, as shown in Figs. 3 and 4. This general behavior is shown for bare CNTs (Fig. 3a), CNTs with 5 ALD cycles (Fig. 3b), and CNTs with 10 ALD cycles (Fig. 3c). During initial loading, a flat surface between the punch face and the pillar top is created. Subsequently, the pillar undergoes elastic loading evident in the initial linear response of the stress strain curve. At a critical stress level, pillar scale buckling occurs, which is reflected in large softening events in the stress-strain curve. This pillar scale buckling moves spatially along the pillar axis with nominally constant stress during the plateau region until it reaches the densification region. The stress rapidly rises in the densification region. The three loading regimes are indicated in Fig. 3c by the highlighted circles. Snapshots of the deformation morphology from the three loading regimes are shown in Fig. 3d.

While the stress-strain curves for the various sample conditions showed self-similar response, images obtained during the compression tests indicate that the ALD coatings substantially altered the pillar scale deformation behavior. For the bare CNT samples, pillar scale buckling occurred at the top of the pillar and moved entirely to the bottom as compression progressed. Buckling initiated at the top likely because the CNTs have more freedom to bend due to frictional interactions with the punch; in contrast, at the bottom CNTs are constrained by bonding to the substrate. In such short CNT micropillars, we also expect that there is a density variation through the height, with a lower density at the top Park et al. (2013b). However, Qiu et al. (2011) performed localized indentation and uniaxial compression experiments recently to show that coordinated buckling of CNT forests is most likely the result of the interplay between the rigid substrate and compliant forest and does not require variation in material properties through the height. Between the first and second buckling (or nucleation) events we could discern an interface marked by arrows in Fig. 3b and c. Above this interface the CNT forests were densified, and below it they were rarefied. The first buckling event remained identical in coated samples. However, for the alumina coated pillars, another buckled region nucleated at the bottom following quasistatic propagation of a portion of the first buckled zone. Notably, this second nucleation of pillar scale wrinkling was not clearly distinguishable in the stress-strain curve, signifying that the deformation mechanism during the plateau region remains the same. An alternative explanation for the second nucleation event is that nonuniformity in the CNT density is augmented by the ALD coating; propagation of the first buckling front may thus compete with nucleation of the second front.

We examined the effect of strain rate on the compressive stress-strain response as shown in Fig. 4. Here, representative stress-strain curves for loading rates from 0.1 to 0.001 s^{-1} are shown in red blue, and green solid lines, respectively, for bare CNTs (Fig. 4a), CNTs with 5 ALD cycles (Fig. 4b), and CNTs with 10 ALD cycles (Fig. 4c), all of which show some strain-rate dependence. However, the qualitative loading response was found to be self-similar regardless of the loading rate.

Digital image correlation (DIC) Eberl et al. (2006) was applied to the SEM images captured during the *in-situ* compression tests to examine the local displacement and strains. The sample with 10 ALD cycles compressed with strain rate of 0.001 s^{-1}, was chosen for the DIC since this sample showed most reliable tracking due to its high contrast features. The SEM images were acquired at one frame per second and subsequently analyzed using DIC

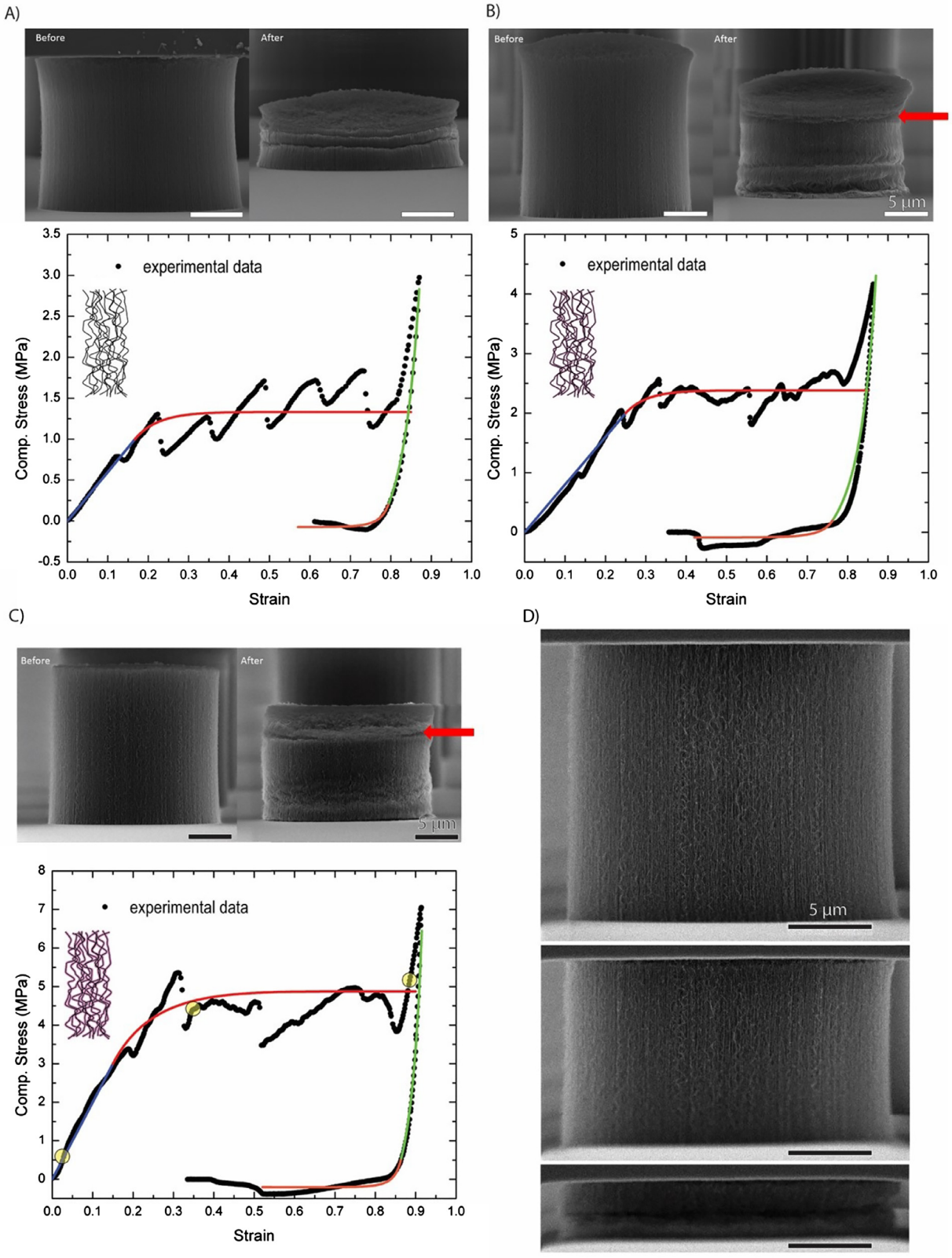

Fig. 3. Quantitative *in situ* uniaxial compressive behavior and SEM images of (a) bare CNTs, (b) CNTs with 5 ALD cycles and (c)CNTs with 10 ALD cycles. An arrow next to the SEM images in (b) and (c) shows the position of the phase boundary above which the forest is densified. The dots in each plot are experimental data and the lines are from the phase transition model. Blue line corresponds to rarefied phase during loading, upper red line to a mixture of rarefied and densified phases during loading, green line to densified phase during unloading, and bottom red line to mixture of rarefied and densified phases during unloading. Note that around a strain of 0.8 there is a difference between the loading and unloading curves (for the densified phase) obtained from experiments. (d) SEM snapshots obtained from the highlighted regions of the stress-strain curve in (c) showing the elastic, plateau, and densification regimes. (For interpretation of the references to color in this figure legend, the reader is referred to the web version of this article.)

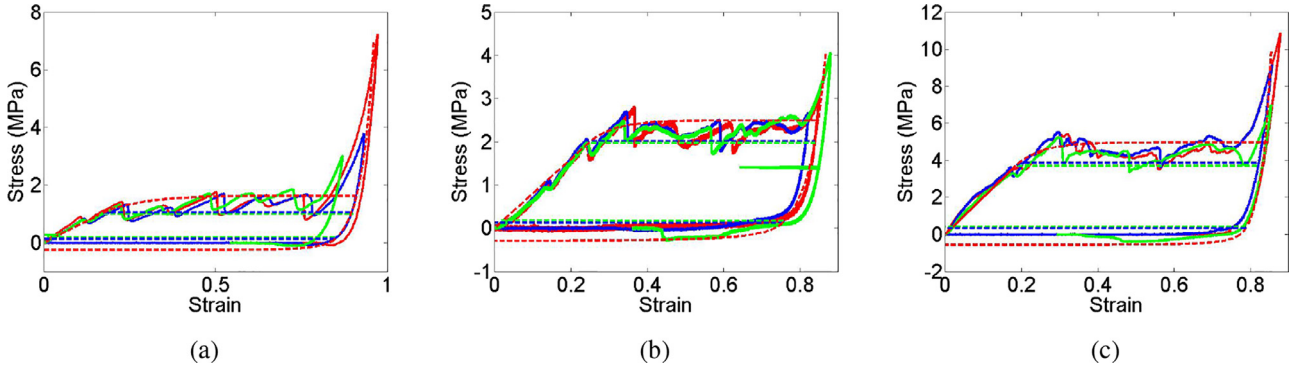

Fig. 4. Compression stress-strain curves for three different strain rates 0.1 s^{-1}, 0.01 s^{-1}, and 0.001 s^{-1} (red, blue, and green solid line respectively) for (a) Bare CNTs, (b) CNTs with 5 ALD cycles, and (c) CNTs with 10 ALD cycles, respectively. Dashed lines are curves predicted by our phase transition model with parameters given in Table 1. (For interpretation of the references to color in this figure legend, the reader is referred to the web version of this article.)

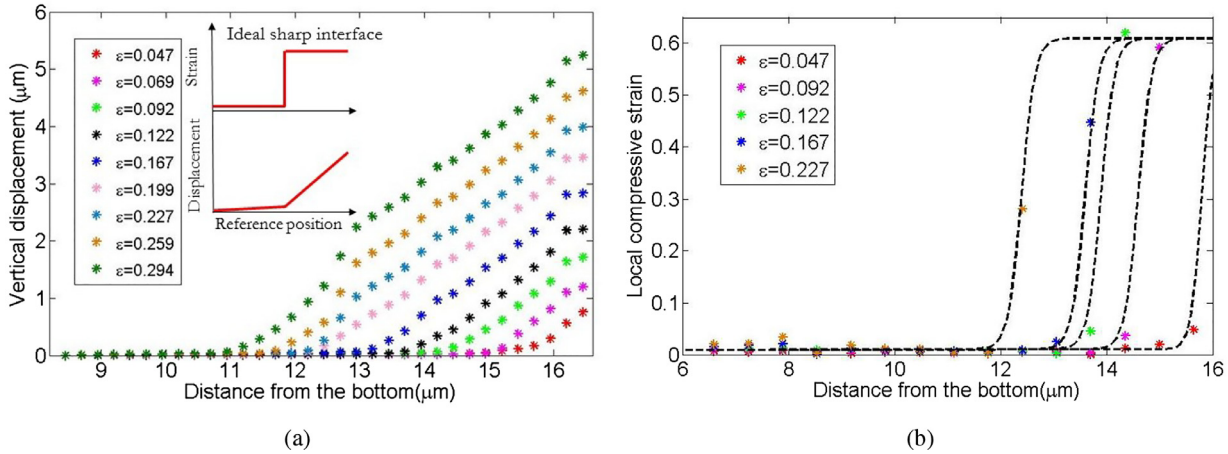

Fig. 5. (a) DIC measurement of displacement at each reference position for various global compressive strains from 0.047 to 0.294. The insets show the piecewise constant strain and piecewise linear displacement profiles for an ideal sharp interface. The experimental displacement profiles look similar to the lower inset. (b) DIC measurement of local strains for various global compressive strains from 0.047 to 0.227 and fitting with Eq. (18).

with an image subset spacing of 250 nm. Longitudinal displacements of the subsets were computed at nine global strain levels, as plotted in Fig. 5a. The longitudinal displacement profiles exhibited approximately the piecewise linear form depicted in the lower inset of Fig. 5a, indicating a clear transition zone. These profiles also demonstrated a shift along the pillar axis with increasing global strain, suggesting the motion of an interface. The longitudinal strain was computed from spatial derivatives of the displacement field (Fig. 5b) for five different global compressive strains, which indicate an interface about 200 nm wide, which also shifts with increasing global strain. Since the width of the interface is much smaller than the height of the sample it can be approximated as a sharp interface, or phase boundary, whose motion is described by a kinetic law.

3.2. CNT forests buckling viewed as a phase transition

Informed by experimental evidence of a phase transformation with a moving phase boundary, we use a one-dimensional quasi-static version of the well-known Abeyaratne–Knolwes theory Abeyaratne and Knowles (2006) for phase transitions in continua to describe CNT pillar compression. The discrete mass-spring model of Fraternali et al. (2011) with bi-stable springs can be thought of as a pre-cursor to our continuum model since it was shown in Purohit (2001) and Zhao and Purohit (2014) that the static and dynamic response of bi-stable chains is analogous to that of one-dimensional phase-transforming continua. In our continuum model the rarefied phase in which the CNTs are mostly straight is described by the stress-strain ($\sigma - \varepsilon$) relation:

$$\varepsilon = \Gamma_L(\sigma), \qquad 0 < \sigma < \sigma_M, \tag{1}$$

where σ_M is the upper stress limit for the rarefied phase. While loading in compression, the densified phase nucleates at a stress $\sigma_{LH} < \sigma_M$, and is described by the stress-strain relation :

$$\varepsilon = \Gamma_H(\sigma), \qquad \sigma_m < \sigma < \infty, \tag{2}$$

where σ_m is the lower stress limit for the densified phase. Similarly, while unloading in compression, the rarefied phase nucleates at stress $\sigma_{HL} > \sigma_m$ (with $\sigma_{HL} < \sigma_{LH}$). Therefore, for $\sigma_m \le \sigma \le \sigma_M$, there are two possible stable phases corresponding to stress σ. We define a transformation strain $\gamma_T(\sigma)$ as:

$$\gamma_T(\sigma) = \Gamma_H(\sigma) - \Gamma_L(\sigma), \qquad \sigma_m \le \sigma \le \sigma_M. \tag{3}$$

We model the compression process of our CNT pillars as an one-dimensional initial-boundary-value problem of a continuum having the above stress-strain relation. We assume that the continuum extends along the x-direction and is confined to the interval $0 < x < L$ in the reference configuration. The displacement of a material point at reference position x is given by $u(x, t)$. The end at $x = 0$ is fixed so that $u(0, t) = 0$ for all t. At the end $x = L$ we apply a displacement boundary condition, so that $u(L, t) = \delta(t)$. We see that when the specimen is being loaded $\dot{\delta}(t) < 0$ and when it is being unloaded $\dot{\delta}(t) > 0$. The equation of motion for our one-dimensional continuum in the quasi-static setting is simply $\partial\sigma/\partial x = 0$, so that $\sigma(x, t)$ is constant for $0 < x < L$ at all t. So,

the state of strain is: $\varepsilon = \Gamma_L(\sigma)$ if $\sigma < \sigma_M$ and $\varepsilon = \Gamma_H(\sigma)$ if $\sigma > \sigma_m$. If the stress σ is such that $\sigma_m < \sigma < \sigma_M$ then a mixture of phases is possible. Consequently, the elongation of the continuum is given by

$$u(L,t) = \delta(t) = \Gamma_H(\sigma(t))s(t) + \Gamma_L(\sigma(t))(L - s(t)), \tag{4}$$

where $s(t)/L$ is the fraction of material in the densified phase (see Fig. 3). Note that if there was a single phase boundary separating the rarefied and densified phases (as is the case before the second nucleation event for all three types of CNT forest) then $s(t)$ denotes the position of the phase boundary in the reference configuration. Recall now that $\delta(t)$ is prescribed, but the evolution of $s(t)$ is as yet unknown. For describing the evolution of $s(t)$, which can be thought of as an internal variable, in this continuum theory we need a kinetic relation Abeyaratne and Knowles (2006). This kinetic relation is expressed in terms of the some driving force f by the relation

$$\dot{s} = \Phi(f(t)), \tag{5}$$

where $\Phi(f)$ is a material property as in Abeyaratne and Knowles (2006). Now, we assume f is a unique function of σ, so the kinetic relation can be expressed as

$$\dot{s} = \bar{\Phi}(\sigma). \tag{6}$$

Differentiating Eq. (4) and eliminating $\dot{s}$ using Eq. (6) we obtain the following equation relating $\sigma(t)$ and $\delta(t)$:

$$\left[p(\sigma) - \gamma_T'(\sigma)\frac{\delta}{L}\right]\dot{\sigma} + \gamma_T(\sigma)\frac{\dot{\delta}}{L} = \frac{\gamma_T^2}{L}\bar{\Phi}(\sigma) \tag{7}$$

where

$$p(\sigma) = \Gamma_L(\sigma)\Gamma_H'(\sigma) - \Gamma_L'(\sigma)\Gamma_H(\sigma). \tag{8}$$

For given $\delta(t)$ Eq. (7) can be integrated to get $\sigma(t)$. In our experiments $\dot{\delta}$ is typically a constant value for both loading and unloading.

3.3. Application to the CNT forests

We now write specific constitutive relations for the stress–strain response of the CNT forests given by Eqs. (1–2), and phase boundary kinetics in Eq. (6). We assume that the stress-strain relation is linear in the rarefied phase as:

$$\sigma = E\varepsilon, \tag{9}$$

if $\varepsilon < \varepsilon_M = \sigma_M/E$, where E is a Young's modulus. In doing so we have assumed that the CNT forests behave as a foam for which the stress-strain response at small strains can be computed in the terms of the properties of single fibers and the density of the network Cao et al. (2005); Zbib et al. (2008); Hutchens et al. (2010); Gibson and Ashby (1999). We point out, however, that density is not the only parameter that determines the Young's modulus of a CNT forest Torabi et al. (2014); Volkov et al. (2009); tortuosity (average curvature of the CNTs) and connectivity (average number of contacts per unit length of CNTs) also play a role, although density dominates the overall modulus Qiu and Bahr (2013). In the densified phase we will start with a non-linear power-law relation given by Van Wyk (1946) and Toll (1998) as :

$$\sigma = kE(\phi^n - \phi_0^n), \tag{10}$$

where k is a coefficient around unity Mezeix et al. (2009), and n is derived to be 3 for three dimensional isotropic random networks Van Wyk (1946); Toll (1998), and also confirmed by several experiments Mezeix et al. (2009); Choong et al. (2013); Bouaziz et al. (2013); Masse and Poquillon (2013); Kim et al. (2015). While vertically aligned CNT forests may be better modeled as transversely isotropic materials, we do not do so here because such a model requires five constitutive parameters which are difficult to meaningfully obtain from uniaxial compression experiments. Furthermore, Hutchens et al. (2012) have demonstrated that an isotropic material model can capture the visco-plastic response quite well. In the above, ϕ_0 is the volume fraction of fibers in the network when $\sigma = 0$ and ϕ is the current volume fraction of the fibers. They are related through the compressive strain ε as

$$\phi = \frac{\phi_0}{1-\varepsilon}, \tag{11}$$

assuming that the cross-sectional area of our specimen does not change significantly (as evident from the images in Fig. 3). This stress-strain relation Eq. (10) does not account for the possibility that fibers can adhere to one another when brought into contact Radhakrishnan et al. (2013); Torabi et al. (2014). In fact, a computational study by Torabi et al. (2014) has revealed that average number of contacts per unit CNT length, or connectivity, depends not just on the fiber volume fraction, but also on the growth process through the seed density (each CNT grows from a seed) and weakly through the cone angle (the limiting cone around link i within which the next link $i+1$ of a growing CNT can lie). Here, in the interest of analytical tractability, we will account for fiber-to-fiber adhesion following Toll (1998) who shows that fiber contact point density scales with the square of the fiber volume fraction $N_c \propto \phi^2$. Assuming each newly formed contact point results in a bond which releases free energy U_{bond}, then the bonding energy per unit volume is $E_{bond} = -C\phi^2 U_{bond}$, where C is a constant. We can add this contribution to the total strain energy stored in the network due to compression and then differentiate the resulting expression to get a new stress-strain law in the densified phase that accounts for adhesion of fibers at contact points, yielding

$$\sigma = kE\left(\phi^3 - \phi_0^3\right) - \frac{2C\phi_0^2 U_{bond}}{(1-\varepsilon)^3} = \frac{B-A}{(1-\varepsilon)^3} - B, \tag{12}$$

where $A = 2CU_{bond}\phi_0^2$, $B = kE\phi_0^3$ are two constants that are obtained by fitting to the experimental stress-strain curves in the densified phase. Finally,

$$\begin{aligned} \Gamma_L(\sigma) &= \frac{\sigma}{E}, \\ \Gamma_H(\sigma) &= 1 - \sqrt[3]{\frac{B-A}{\sigma+B}}, \\ \gamma_T(\sigma) &= 1 - \sqrt[3]{\frac{B-A}{\sigma+B}} - \frac{\sigma}{E} \end{aligned} \tag{13}$$

A similar exercise accounting for contacts with adhesion was also performed by Hutchens et al. (2012), but they simplified the resulting expressions to modify the visco-plastic hardening law in the plateau region of the stress-strain curve. We can use the results above to derive an expression for the driving force f in the quasi-static limit. We know from Abeyaratne–Knowles Abeyaratne and Knowles (2006) that:

$$f(\sigma) = \int_{\sigma_0}^{\sigma} \gamma_T(\sigma')\, d\sigma', \tag{14}$$

where σ_0 is a Maxwell stress. Recall that at the Maxwell stress, the Helmholtz free energy density of the two phases is equal. The driving force f derived above enters a kinetic relation describing the evolution of the internal variable $s(t)$. For simplicity we use the following kinetic relation:

$$\dot{s} = \Phi(f) = \begin{cases} M_{LH}(f - f_{LH}), & \text{if } f > f_{LH}, \\ 0, & \text{if } f_{HL} \le f \le f_{LH}, \\ M_{HL}(f - f_{HL}), & \text{if } f < f_{HL}. \end{cases} \tag{15}$$

Here $M_{LH} > 0$ and $M_{HL} > 0$ are mobility parameters which we will later fit to the experimental data. Also, f_{LH} and f_{HL} correspond,

Table 1
Fitting parameters for the uniaxial compression experiment.

Group	E(MPa)	B(MPa)	A(MPa)	σ_{LH}(MPa)	σ_{HL}(MPa)	M_{lh}(MPa^{-1}s^{-1})	M_{hl}(MPa^{-1}s^{-1})
Bare CNT	6	0.67	0.66	1	0	0.35	0.3
ALD 5 cycle	8	0.61	0.60	2	0.2	0.5	0.3
ALD 10 cycle	20	1.37	1.36	3.7	0.5	0.09	0.12

respectively, to stresses σ_{LH} and σ_{HL} which may be determined using Eq. (14)s. Our justification for choosing such a "stick-slip" type kinetic relation is as follows. We know from earlier work that thermal sliding of contacts between CNTs occurs when a CNT forest is compressed Radhakrishnan et al. (2013); Mesarovic et al. (2007). Thermally activated processes are governed by Arrhenius type kinetics which can be linearized for small driving forces to give a linear kinetic law of the type $\dot{s} = Mf$ where M is a constant Abeyaratne and Knowles (2006). We also know from computations Torabi et al. (2014); Volkov et al. (2009) and experiments Qiu et al. (2011) that the CNTs reorient as the forest transforms from a rarefied phase to the densified phase. The kinetics of the reorientation is difficult to obtain, but it is clear that these processes produce a material that is heterogeneous at length scales much smaller than the specimen size. It has been shown that this sort of heterogeneity combined with a linear kinetic law at the microscopic scale leads to a stick-slip type of kinetic relation at the macroscopic scale Bhattacharya (1999). That said, the choice of kinetic relation above is not sacrosanct; the appropriate kinetic law should be deduced by fitting to experiment or nanoscale computations. The kinetic law, Eq. (15), fits the experiments described here quite well (as shown later).

In order to complete the formulation of the problem, we need a nucleation criterion. For loading, when the specimen is being compressed, the densified phase nucleates in the rarefied phase at stress σ_{LH} where σ_{LH} can be assumed to be where driving force f is just greater than f_{LH} so that the phase boundary makes its appearance and immediately moves. Similarly, for unloading, the rarefied phase nucleates in the densified phase at stress σ_{HL} where driving force f is just smaller than f_{LH}.

The experiment is performed at a constant rate $\dot{\delta} < 0$ during loading. Initially, the entire continuum is in the rarefied phase. As the compressive strain ε increases, the stress σ increases linearly and reaches the critical value σ_{LH}; this is when a phase boundary nucleates at the top of the CNT pillar ($x = L$), with the densified phase on its top and the rarefied phase on its bottom. The stress in the continuum is now governed by Eq. (7) with initial condition $\sigma = \sigma_{LH}$ given by the nucleation criterion. The kinetic relation enters the mechanics through $\bar{\Phi}(\sigma)$. The phase boundary moves through the continuum and converts all the material into the densified phase. Once the phase boundary has reached $x = 0$, Eq. (7), the nucleation criterion and the kinetic relation are no longer required. The stress is the determined by the constitutive law $\Gamma_H(\sigma)$ since all the material is in the densified phase. When we unload $\dot{\delta} > 0$, the stress declines along the curve $\Gamma_H(\sigma)$ until a critical value σ_{HL} is reached at which a phase boundary nucleates at $x = 0$. Then $\sigma(t)$ is again governed by Eq. (7) with initial condition $\sigma = \sigma_{HL}$. This differential equation remains relevant until the phase boundary has traversed the full length of the specimen reaching $x = L$. After this, the stress follows the curve $\Gamma_L(\sigma)$ in the rarefied phase.

We have fitted the experimental data in Fig. 3 from the measured loading and unloading response of three different samples using the methods described above. In Fig. 3, the experimental data is represented by discrete markers and the model fit is shown as a continuous line. The strain rate $\dot{\delta}/L$ for these experiments was 0.001 s^{-1}. The parameters obtained from the fits are summarized in Table 1. Our phase transitions model captures the main features of the stress-strain curve quite well. The fitting parameters are E of the rarefied phase, two constants A and B of the densified phase (recall that A captures the release of free energy per adhesive bond and B is a modulus with units of stress for the densified phase), σ_{LH} and M_{LH} for the upper plateau and σ_{HL} and M_{HL} in the lower plateau. The theoretical lines fall on top of the experimental data for the linear elastic response in the rarefied phase and the non-linearly elastic response in the densified phase. The plateaus in loading/unloading are also captured except for the stress-jumps seen in the loading plateau, on which we will comment later. We note that the Young's moduli in the rarefied phase of the bare CNT pillars is the smallest. The Young's modulus in the rarefied phase increases as the thickness of the ALD alumina coating increases. Similarly, the stress at which the densified phase nucleates is also lowest for the bare CNTs and it increases as the thickness of the ALD layers increases. This is expected since increasing the thickness of the CNTs increases their stiffness causing an increase in the Young's modulus in the rarefied phase. The densified phase is nucleated when the fibers buckle. The critical stress σ_{LH} is determined for foams from a knowledge of the buckling load of single fibers and the density of the network. For example, in Cao et al. (2005) the critical stress for buckling of a foam with CNT volume fraction of 13% was 12 MPa, so critical stress for buckling of a single nanotube was estimated to be about 12 MPa/0.13 $\approx$ 92 MPa. In our bare CNT samples we estimate that the diameter of the CNTs is $d \approx 10$ nm and the spacing between adjacent CNTs is $D \approx 100$ nm, on average. Thus, $\phi_0 \approx (d/D)^2 \approx 0.01$. The buckling stress σ_{LH} for the bare CNT pillars in our experiments was about 1 MPa, so that the critical stress for buckling of a single nanotube is approximately $\sigma_{LH}/\phi_0 = 1$ MPa/0.01 $\approx$ 100 MPa which is in the same range as that of Cao et al. (2005). If the bending stiffness is higher due to increased thickness of the ALD layers then σ_{LH} also must increase. This is exactly what we see in fitting our model to the experimental data.

It is difficult to assess the reasonableness of the mobility parameters M_{LH} and M_{HL} as they have not been measured previously in experiments. However, we can predict the stress–strain response in loading/unloading of the same samples at different strain rates $\dot{\delta}$. We have done this exercise for two other strain rates (0.01 s^{-1} and 0.1 s^{-1}) with the parameters shown in Table 1. The corresponding experimental stress-strain curves for these strain-rates are plotted together with the theoretical predictions in Fig. 4. Remarkably, the agreement between theory and experiment indicates that the parameters we have obtained from fitting one set of experimental data are useful in describing the constitutive response of the material at other strain-rates as well. In particular, the nucleation stresses and our choice of the kinetic law gives a small strain-rate dependence of the hysteresis which is consistent with earlier experiments Pathak et al. (2012); Raney et al. (2013a); 2013b). If the motion of the phase boundary was independent of the stresses then our model would reduce to the rate-independent hysteresis models of Fraternali et al. (2011); Blesgen et al. (2012); Raney et al. (2013a); 2013b).

Finally, we point to an important feature that has not been captured by our phase transition model described above. Note in Fig. 3 and Fig. 4 that near a strain of 0.8 (which corresponds to

Table 2
Change of phase fractions at stress jumps.

Group	Number of jumps studied	Δs(μm)
Bare CNTs	9	0.27± 0.09
CNTs with 5 ALD cycles	6	0.21± 0.1
CNTs with 10 ALD cycles	8	0.20± 0.16

most of the pillar being in the densified phase) the experimental loading and unloading curves are not identical at the end of loading. This was observed in simulations of fiber networks by Barbier et al. (2009) and attributed to friction between contacting fibers. In our experiments, the increased contact between the CNTs in the densified phase exacerbates this effect. In fact, the loading and unloading curves in our nanoindentation experiments are also different, indicating dissipation.

3.4. Stress jumps at the plateau, buckling wavelength and interfacial energy

Our constitutive model yields a plateau in the stress-strain curve that is smooth. This is not what we see in experiments. In fact, the stress-plateau in the experimental data invariably has a few jumps in the stress (shown in Fig. 4 for various strain rates), which are caused by nucleation of the densified phase away from the moving phase boundary. In this section we will quantify these jumps using Eq. (4). For each jump the phase fraction $s(t)$ changes suddenly and we can estimate the phase fractions from the strains before and after the jumps using:

$$s_- = \frac{\delta_-/L - \Gamma_L(\sigma_-)}{\Gamma_H(\sigma_-) - \Gamma_L(\sigma_-)}, \qquad s_+ = \frac{\delta_+/L - \Gamma_L(\sigma_+)}{\Gamma_H(\sigma_+) - \Gamma_L(\sigma_+)}. \tag{16}$$

where the subscript $-, +$ indicates variables before and after the jump, respectively. We will denote $\Delta s = s_+ - s_-$. Using Eq. (16), we estimate Δs from all visible stress jumps in the experimental data in Fig. 4. We present the results in Table 2.

The above analysis assumed that the interface is sharp (a discontinuity in strain $\varepsilon(Z)$), but in experiments the interface is diffuse with a continuous $\varepsilon(Z)$. Such diffuse interfaces between the rarefied and densified phases have been characterized using viscosity-strain gradient models for phase boundaries described in Abeyaratne and Knowles (2006) and references therein. For example, Turtletaub (1997) augments the Helmholtz free energy density of a phase changing material with an interfacial energy density term $\frac{\lambda}{2}\left(\frac{d\varepsilon}{dx}\right)^2$ where λ is the strain-gradient or capillarity parameter. In such a theory for phase boundary motion one then looks for a traveling wave solution (moving at velocity V_n) of the regularized equations as discussed in Abeyaratne and Knowles (2006) and references therein. If the stress-strain relation of our CNT forests is modeled as a cubic $\sigma - \sigma_0 = \alpha(\varepsilon - \varepsilon_*) - \beta(\varepsilon - \varepsilon_*)^3$ then a viscosity-strain gradient model Abeyaratne and Knowles (2006) with $V_n = 0$ and λ as the strain-gradient or capillarity parameter gives a differential equation for $\epsilon(Z) = \varepsilon(Z) - \varepsilon_*$:

$$\lambda \frac{d^2\epsilon}{dZ^2} + \alpha\epsilon - \beta\epsilon^3 + \sigma - \sigma_0 = 0. \tag{17}$$

The solution to this differential equation is

$$\epsilon(Z) = \varepsilon(Z) - \varepsilon_* = a + b\tanh\left(\frac{Z - Z_0}{c}\right), \tag{18}$$

when the remote conditions at $\pm\infty$ are constant strains $\varepsilon(\infty) = a + b$ in the densified phase, and $\varepsilon(-\infty) = a - b$ in the rarefied phase. We fit the experimental strain profiles $\varepsilon(Z)$ for the 10 ALD cycles pillars in the Fig. 5b using Eq. (18) and obtain $a = 0.31$, $b = 0.3$, $c = 0.2$ μm. This is a relatively sharp interface, consistent with the displacement profiles shown in Fig. 5a. We performed similar calculations on the CNT compression experiments in Maschmann et al. (2012) and obtained $a = 0.315$, $b = 0.3$, $c = 2$ μm from fits to the experimental strain profiles in Fig. 5(b) of Maschmann et al. (2012).

The interface width, $2c$, is directly proportional to the buckling wavelength. According to Zbib et al. (2008) the presence of this buckling wavelength indicates that a continuum model with an intrinsic material length scale is required to model CNT forests. How this internal length scale depends on statistical parameters of the CNT forest was investigated by Torabi et al. (2014) who showed that the buckling wavelength depends on tortuosity K, density l and connectivity γ (these are symbols used in Torabi et al. (2014)) in the undeformed state. They deduced an empirical relation $c\sqrt{l} = \beta_1 + \beta_2\gamma/K$ where β_1, β_2 are constants. On the other hand, the buckling stress σ_b in Torabi et al. (2014) increased linearly with increasing l and was only weakly dependent on γ/K. Thus, we expect from Torabi et al. (2014) that c should vary inversely with σ_b. Now, in our CNT forests with 10 ALD cycles c = 0.2 μm and $\sigma_b \approx$ 4.5 MPa (for bare CNT forests $\sigma_b \approx 1.3$ MPa), while in Maschmann et al. (2012) $c = 2$ μm and $\sigma_b \approx 0.6$ MPa. The inverse relationship between σ_b and Δs (Δs is proportional to c) can also be seen in Table 2 and Table 1. Thus, our results for trends in c vs. σ_b are consistent with those of Torabi et al. (2014). Torabi et al. (2014) relate c to tortuosity, density and connectivity, all of which should increase as we cross the interface from the rarefied to the densified phase, while we surmise that c is connected to the interfacial energy in the viscosity-strain gradient model described, for example in Turtletaub (1997), and other references in Abeyaratne and Knowles (2006). Intuitively, these two descriptions of the intrinsic length scale are not unrelated – interfacial energy arises because the environment of a material point on the two sides of an interface are different Israelachvili (2011). A final point to note is that the interfacial energy depends on the square of the strain-gradient in the viscosity-strain gradient model of Turtletaub (1997). Strain-gradient elasticity theories Toupin (1962); Koiter (1964); Mindlin and Eshel (1968) in which the elastic energy depends quadratically on both strains and strain-gradients naturally have intrinsic length scales.

4. Indentation of CNT forests

The experiments and analysis discussed thus far have resulted in a micro-structurally motivated continuum model based on the mechanics of foams and the theory of phase transitions. Our goal now is to test the applicability of this model by using it to interpret nanoindentation experiments (Fig. 2d) on the same materials.

4.1. Experiment

The nanoindentation experiments were performed using a Hysitron®TI-950 Triboindenter™, fitted with a conical diamond indenter tip with spherical end. As shown in Fig. 2d, the indenter has a radius of about 1μm and an included angle of 90°, which is much smaller than the height and diameter of the CNT pillars (both 20 μm). We performed a series of loading and partial unloading tests with controlled peak load as shown in Fig. 6a. Specially, there were 10 cycles of loading and unloading at each location. In each cycle, except the last cycle, the load was ramped up to a fixed peak load in 2s and then unloaded to 5% of its peak load in another 2s (see Fig. 6a inset). In the last cycle, the sample was fully unloaded and the indenter was completely withdrawn from the surface. The peak load was increased uniformly from 5μN up to 50μN. Three different samples, i.e. bare CNT, and 5 and 10 cycles

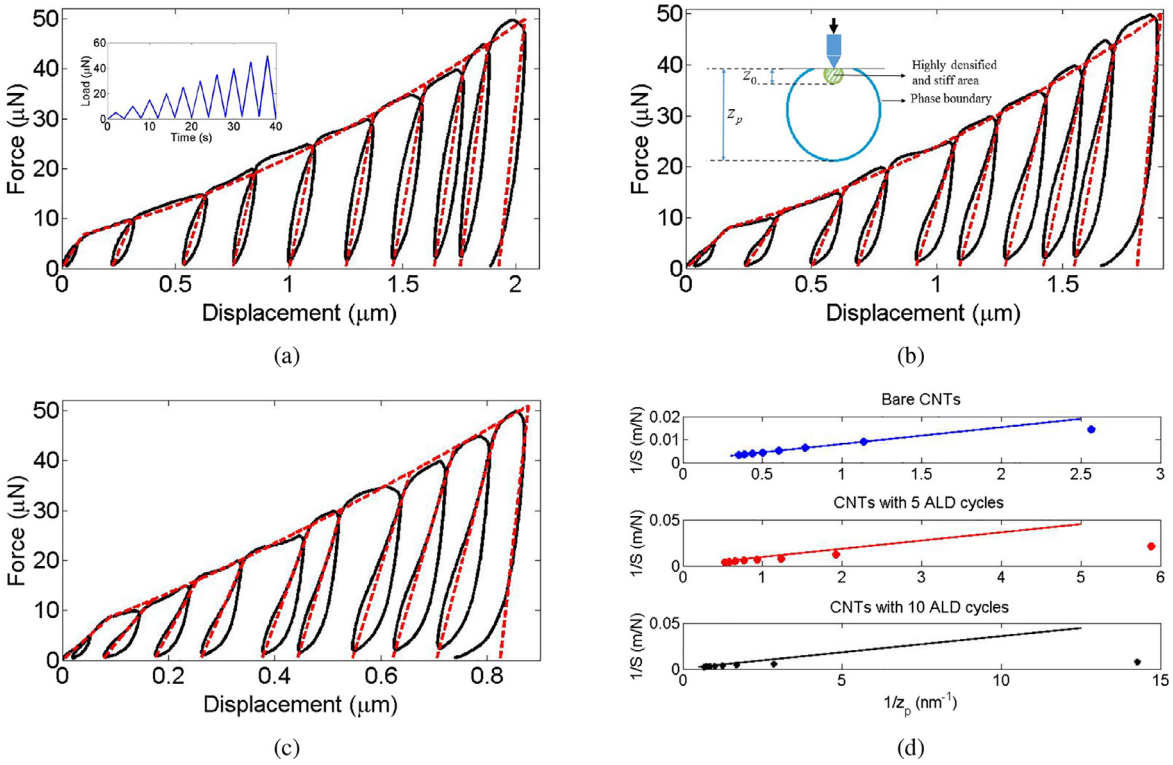

Fig. 6. (a) Force-displacement curve for a bare CNT pillar in a nanoindentation experiment (black solid line). The inset shows the scheme of loading and unloading cycles in our nanoindentation experiment. (b) Force-displacement curve for a CNT pillar with 5 ALD cycles in a nanoindentation experiment. The inset is a figure showing the position z_0 and phase boundary z_p used in calculating the displacement underneath the point load. (c) Force-displacement curve for a CNT pillar with 10 ALD cycles in a nanoindentation experiment. Note that hysteresis increases with increasing load in panels a,b,c. There is a residual displacement at the end of each unloading. The red dashed lines through the peak loads in panels a,b,c are fits using Eq. (26) which combines the Boussinesq solution and a phase transition model. The slope of the red dashed lines through the loops in panels a,b,c are the experimental stiffnesses S. (d) Plots of $1/z_p$ versus $1/S$ for each loading/unloading loop, respectively for bare CNTs, CNTs with 5 ALD cycles, and CNTs with 10 ALD cycles. Solid lines are from Eq. (27)s with parameters E_1, E_H, and z_0 from Table 3. (For interpretation of the references to color in this figure legend, the reader is referred to the web version of this article.)

of ALD coated CNT pillars, were measured. For each material, 6 different pillars were tested. The indentation tests were always performed at the center of each individual pillar. Force-displacement curves were collected during experiments. One such curve each is shown as the black solid line in Fig. 6a for bare CNT, Fig. 6b for CNTs with 5 cycles ALD coating and Fig. 6c for CNTs with 10 cycles ALD coating. Notice that there is hysteresis in each cycle of loading/unloading and it increases at larger forces. This is true for bare CNTs, as well as CNTs with 5 ALD cycles and CNTs with 10 ALD cycles. Also notice that the residual displacement at zero load at the end of each cycle keeps increasing as the peak load increases. We show below that this is a consequence of the phase transition in the CNT forest.

4.2. The Hertz contact solution

Since our indenter has a spherical tip, we first assess if the Hertz contact solution can provide an adequate description of our experiments. Recall that for the Hertz solution the contact radius a, the indentation depth δ and the maximum pressure p_0 are related through Johnson (1985)

$$a = \left(\frac{3PR}{4E^*}\right)^{1/3}, \qquad \delta = \left(\frac{9P^2}{16RE^{*2}}\right)^{1/3}, \qquad p_0 = \left(\frac{6PE^{*2}}{\pi^3 R^2}\right)^{1/3}, \tag{19}$$

where R is the radius of the indenter, P is the load and

$$\frac{1}{E^*} = \frac{1-\nu_{in}^2}{E_{in}} + \frac{1-\nu_{hs}^2}{E_{hs}}, \tag{20}$$

where E_{in}, ν_{in} are the Young's modulus and Poisson ratio of the indenter and E_{hs}, ν_{hs} are those for the half-space. In our experiments E_{in} is very large in comparison to E_{hs} and $\nu_{hs} \approx 0$, so we take $E^* = E_{hs}$. For small loads P we expect that the entire half-space will be in the rarefied phase which is modeled as a linear elastic material with Young's modulus E. When the pressure p_0 reaches a critical value $\sigma_C = \sigma_{LH}$ then the densified phase should nucleate right underneath the indenter. For bare CNTs we take $E = 6$ MPa (see Table 2), we know from experiments that $R = 1\mu$m, so we estimate $P = 0.14\mu$N when $p_0 = \sigma_{HL} = 1$ MPa. At $P = 0.14\mu N$, Eq. (19) gives $a = 0.26\mu$m and $\delta = 0.068\mu$m. The Hertz solution is a good approximation to the contact problem of a spherical indenter on a half-space for $a/R < 0.1$, and according to Yoffe (1984), can lead to logical inconsistencies if applied outside the range $a/R < 0.2$. As we violate these limits at a load of 0.14μN which is smaller than most of the loads in the experiments, the Hertz solution is clearly not suitable. Our problem involves a phase transition, so the corrections to the Hertz solution detailed in Yoffe (1984) and based on first-order linear elasticity also cannot be applied. Thus, we analyze the problem with a point load on a half-space. As detailed below the point load approximation is more appropriate for large values of P for which the ratio of indentation depth to indenter radius, $\delta/R > 1$. The contact problem could also be analyzed using the finite element method but this is beyond the scope of the current work.

4.3. Point load on a half-space capable of phase transitions

The indenter is small compared to the sample size (1/20), thus we approximate the indentation test using the Boussinesq solution

Table 3
Fitting parameters for nanoindentation experiment.(The error-bars account for distinct nanoindentation groups.)

Group	Bare CNTs	CNTs with 5 ALD cycles	CNTs with 10 ALD cycles
z_0(μm)	1.8	1.38	1.06
E_1(MPa)	6.14± 0.42	5.44± 1.01	13.30± 1.11
E_H(MPa)	38.82± 0.89	62.76± 1.58	111.11± 2.33
γ_T (indentation)	0.562± 0.007	0.655± 0.044	0.362± 0.026

for a half-space with a point-load as in Craig (2013). The load is applied perpendicular to the surface of the half-space and the displacement underneath the load for a homogeneous half space is given by:

$$u = \frac{3P}{2\pi Ez}, \tag{21}$$

where P is the applied point load, z is the depth from the surface and E is a reduced modulus with effect of Poisson ratio included. The stress distribution $\boldsymbol{\sigma}(r, z)$ within the half space for this axisymmetric problem is given by:

$$\begin{aligned}
\sigma_z &= \frac{3Pz^3}{2\pi R^5},\\
\sigma_r &= \frac{P}{2\pi R^2}\left[\frac{3r^2 z}{R^3} - \frac{(1-2\nu)R}{R+z}\right],\\
\sigma_\theta &= \frac{(1-2\nu)P}{2\pi R^2}\left[\frac{R}{R+z} - \frac{z}{R}\right],\\
\tau_{rz} &= \frac{3Prz^2}{2\pi R^5}.
\end{aligned} \tag{22}$$

where r is reference radius in the polar coordinate system, and $R = \sqrt{r^2+z^2}$. This solution is valid for infinitesimal strains and isotropic linear elastic materials. However, the CNT forests we study are capable of phase transitions. Hence, underneath the applied load, where the stresses are very large, we expect that the CNT forests will be in the densified phase as shown in Fig. 2a. In order to accommodate this possibility we replace Eq. (10) in the densified phase with a linearized version

$$\Gamma_H(\sigma) = \gamma_T + \sigma/E_H, \tag{23}$$

where the modulus E_H in the densified phase is much larger than that in the rarefied phase. This simplifying assumption enables us to exploit the Boussinesq solution. Since we know the expression for the stress σ_z in the Boussinesq solution the location of the phase boundary (r, z) for given P is determined by setting σ_z (from Eq. (22)) equal to a critical stress of nucleation σ_C, or:

$$3Pz^3 = 2\pi\sigma_C\left(r^2+z^2\right)^{\frac{5}{2}}. \tag{24}$$

This critical stress σ_C is taken to be σ_{LH} in compression and the shape of a typical phase boundary described by Eq. (24) is shown in the inset of Fig. 6b. As the load increases, the phase boundary will move deeper into the half space, and thus the region containing the densified phase will increase its volume. There is a jump in strain across this phase boundary, but there is no jump in stress since the phase boundary moves in a quasi-static manner. Since the expressions in Eq. (22) for the stress field are not a function of the Young's modulus and we assume that the material is linear elastic in both phases, they are valid on both sides of the phase boundary.

Next, we must obtain an expression for the normal displacement along the center line ($r = 0$). Let $z = z_p$ ($0 \le z$, $z_p < \infty$) be the position of the phase boundary along $r = 0$. For $z > z_p$ (along $r = 0$) the CNT forest is in the rarefied phase for which $\varepsilon_z = \frac{\sigma_z}{E_1}$ where E_1 is a Young's modulus, while for $z < z_p$ the CNT forest is in the densified phase for which we have used a linearized stress-strain relation Eq. (23). Due to the symmetry of the problem the displacement $u(0, z)$ for a point z ($z < z_p < \infty$) along $r = 0$ can be obtained by integrating $\varepsilon(0, z)$ as follows:

$$\begin{aligned}
u(0,z) &= \int_{z_p}^{\infty}\frac{\sigma_z}{E_1}\,dz + \int_z^{z_p}\left(\frac{\sigma_z}{E_H}+\gamma_T\right)dz\\
&= \frac{3P}{2\pi}\left(\frac{1}{E_1 z_p} + \frac{1}{E_H z} - \frac{1}{E_H z_p}\right) + \gamma_T(z_p - z).
\end{aligned} \tag{25}$$

We see that $u(0, z) \to \infty$, as $z \to 0$. This happens because the linearized stress-strain law Eq. (23) is valid only for $0 \le \sigma_z \le E_H(1-\gamma_T)$, while $\sigma_z \to \infty$, as $z \to 0$ along $r = 0$ in the point load solution. If in the integral for $u(0, z)$ above we use the fully non-linear stress-strain law for the densified phase, Eq. (10) instead of Eq. (23), then the displacement $u(0, 0)$ does not blow up even though $\sigma_z(0, 0)$ becomes infinite. To correct for our use of the linearized stress–strain law Eq. (23) for the high strain phase, we introduce a position z_0 and compute δ underneath the load as

$$\delta = \frac{3P}{2\pi}\left(\frac{1}{E_1 z_p} + \frac{1}{E_H z_0} - \frac{1}{E_H z_p}\right) + \gamma_T(z_p - z_0). \tag{26}$$

z_0 is the depth along the center line where $\sigma_z(0, z_0) = \sigma_{LH}$ for the P at which the load-indentation depth curve suddenly changes slope (around 8μN) for all samples. By using Eq. (26) to compute displacements underneath the load we are assuming tacitly that the CNT forest above this reference position z_0 is in a highly densified and stiff state due to large stresses (see the inset of Fig. 6b), so that the displacement at z_0 is nearly equal to the displacement underneath the indenter. We will use Eq. (26) to interpret our nanoindentation data on the CNT forests. A consequence of Eq. (26) is that the stiffness (slope of the load versus indentation depth curve) changes as z_p changes.

In the experiments each sample is loaded and unloaded in a cyclic manner according to the protocol shown in the inset of Fig. 6a. In the first cycle the load is increased at a constant rate up to P_1, and then it is decreased to nearly zero at a constant rate. In the second cycle the same protocol is followed but the maximum load is $P_2 > P_1$. In the third cycle the maximum load is $P_3 > P_2$, and so on for all subsequent cycles. A typical load indentation curve is plotted in Fig. 6a as the black line. Notice that there is a change in the slope of the line at $P \approx 8$μN, due to softening, presumably caused by the phase transition. We determine z_0 for this sample by setting $\sigma_z(z_0) = \sigma_c$ at $P \approx 8$μN. σ_c are chosen based on the nucleation stress σ_{LH} in Table 2, respectively, for the three different CNT pillars, and the calculated z_0 are reported in Table 3. For $P > \approx 8$μN the phase boundary moves to $z_p > z_0$ along the line $r = 0$ (shown in the inset of Fig. 6b). During unloading, the phase boundary does not move inward because of our choice of the kinetic relation and also because the nucleation stress for the rarefied phase is very small as can be seen in Table 1. Hence, the phase boundary remains static and the region inside is unloaded along the stress-strain curve of the densified phase. Therefore, the slope of the re-loading curve is larger than the initial loading curve.

When the load is reduced to zero, there is some residual deformation due to the transformation strain γ_T in Eq. (26) above.

When the load is increased again the phase boundary moves outward only when the load exceeds P_1, and it stops when the peak load $P = P_2$ is reached. Hence, we can compute the new z_p for the second re-loading curve. By following the same procedure for all the loading/unloading cycles we can predict the indentation depths for the peak loads P_2, P_3, P_4, .., etc. Since we use the point load solution we have fitted E_1, E_H and γ_T in Eq. (26) to match the indentation depths at the peak loads $P_1, P_2, P_3, \ldots$ etc., and the last unloading curve from a peak load of 50μN. The resulting parameters are shown in Table 3 for the three different materials and typical experimental curves with fits appear in Fig. 6a for bare CNTs, Fig. 6b for CNTs with 5 ALD cycles and Fig. 6c for CNTs with 10 ALD cycles. We see that the values of E_1 are close to E obtained from fitting the uniaxial compression data. The transformation strains γ_T are close to the magnitude of the strain jumps at the stress plateaus for each of the three types of CNT pillars and the trend in the E_H values indicates that the Young's modulus in the densified phase increases as the ALD alumina coating thickness increases. In the appendix we use a linear stress-strain relation for the densified phase to refit the uniaxial compression experimental data and obtain Young's modulus of both rarefied and densified phases E_L, E_H respectively, and transformation strain γ_T. We compare them with the same parameters extracted from fitting the nanoindentation experiments and find that all of them are consistent. This shows that the same phase transition model can quantitatively describe both uniaxial compression as well as nanoindentation experiments.

As a test of our analysis we consider the slope S of our load-indentation depth curve. The slope S (during unloading when z_p remains fixed) can be obtained from Eq. (26) as

$$S = \frac{2\pi}{3}\left[\frac{1}{E_1 z_p} + \frac{1}{E_H z_0} - \frac{1}{E_H z_p}\right]^{-1}. \tag{27}$$

As the phase boundary goes deeper into the half-space, Eq. (27) reveals that the stiffness increases. The increase in stiffness is expected because more densified phase is created as we go to higher loads. To test Eq. (27) we first extract the experimental stiffnesses S for each loading/unloading loop by drawing a line through the point where the loading and unloading curves intersect and the point at the bottom of each loop in Fig. 6a, 6 b and c. We then plot $1/S$ as a function of $1/z_p$ in Fig. 6d for each of the three materials. The lines in each panel are those expected from Eq. (27) with parameters from Table 3. We find that the agreement between the experimental stiffnesses and Eq. (27) is reasonable for low values of $1/z_p$, or for large values of z_p which happen at large values of P. Also, the agreement is best for bare CNTs in which we get the highest indentation depths. Thus, our analysis based on a point load solution agrees well with experiment when the indentation depths are larger than the indenter radius, which is not entirely unexpected.

5. Conclusion

In this paper we have shown that a model for phase transitions in continua can describe the deformation of CNT forests both in uniaxial compression and nanoindentation experiments. We have used specialized constitutive laws in the rarefied and densified phases that are based on the bending of individual fibers. We have modified well-known models for the compression of fiber networks in the densified phase to account for sticking of the fibers. Some features in our model, such as, rate-dependence and fiber-to-fiber adhesion are also present in the models of Hutchens et al. (2011, 2012), but we describe reversible deformations with hysterisis, while Hutchens et al. focus on irrecoverable deformation. Our model also shares some features with those of Fraternali et al. (2011); Blesgen et al. (2012), such as, the multi-well energy landscape of the springs. However, our's is a continuum model which can be used to study a broader class of materials and mechanical behaviors (see, for example, Kim et al. (2015) where we apply similar ideas to fibrin networks). We have exemplified this by performing experiments on ALD alumina coated CNT pillars and shown how their mechanical parameters are affected by ALD coating thickness (Davami et al., 2016). Our model could eventually be used to further understand the structure-property relationships of CNT forests, and therefore to design CNT forest morphologies to have tailored mechanical response.

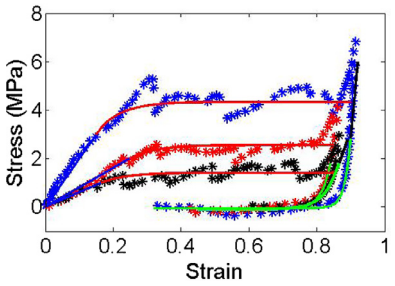

Fig. 7. Fitting of compression experiment using a linear stress-strain relation in densified phase for bare CNT (black dots), CNTs with 5 ALD cycles (red dots) and CNTs with 5 ALD cycles (blue dots). The lines are obtained from the phase transition model with parameters listed Table 4. The blue line corresponds to specimen in the rarefied phase, red line to a mixture of rarefied and densified phases during loading, black line to densified phase and green line to a mixture of rarefied and densified phases during unloading. (For interpretation of the references to color in this figure legend, the reader is referred to the web version of this article.)

Acknowledgments

This work was funded in part through the National Science Foundation under awards DMR-1120901, CMMI-1463344, and CMMI-1463181. The microcompression testing was supported by the U.S. Department of Energy, Office of Basic Energy Sciences, Division of Materials Science and Engineering under Award #DE-SC0008135.

Appendix

Fitting the uniaxial compression experiment using a piece-wise linear stress–strain relation

Our goal here is to show that a piece-wise linear stress-strain law, like the one we used to describe the nano-indentation experiment, can also quantitatively capture the stress-strain plots of the uniaxal compression experiments. In the main text we had used a non-linear relation to model the densified phase which we could not exploit in the solution of the Boussinesq problem for nanoindentation. A piece-wise linear stress-strain relation for the rarefied and densified phases is:

$$\begin{aligned} \Gamma_L(\sigma) &= \frac{\sigma}{E_L}, \\ \Gamma_H(\sigma) &= \gamma_T + \frac{\sigma}{E_H}, \end{aligned} \tag{28}$$

We have used this to refit the compression experiment in Fig. 7. The fitting parameters are summarized in Table 4. We compare them with the same parameters from nanoindentation and show consistency.

Table 4
Comparison of linear phase transition model parameters used in nanoindentation vs uniaxial compression.

Group	Bare CNTs	CNTs with 5 ALD cycles	CNTs with 10 ALD cycles
E_L(MPa) (indentation)	6.14± 0.42	5.44± 1.01	13.30± 1.11
E_l(MPa) (compression)	6	8	20
E_H(MPa) (indentation)	38.82± 0.89	62.76± 1.58	111.11± 2.33
E_H(MPa) (compression)	40	60	150
γ_T (indentation)	0.562± 0.007	0.655± 0.044	0.362± 0.026
γ_T (compression)	0.747	0.70	0.76

References

Abeyaratne, R., Knowles, J.K., 2006. Evolution of phase transitions: a continuum theory. Cambridge University Press.

Barbier, C., Dendievel, R., Rodney, D., 2009. Role of friction in the mechanics of nonbonded fibrous materials. Phys. Rev. E 80 (1), 016115.

Bedewy, M., Meshot, E.R., Hart, A.J., 2012. Diameter-dependent kinetics of activation and deactivation in carbon nanotube population growth. Carbon N Y 50 (14), 5106–5116.

Bedewy, M., Meshot, E.R., Reinker, M.J., Hart, A.J., 2011. Population growth dynamics of carbon nanotubes. ACS Nano 5 (11), 8974–8989.

Bhattacharya, K., 1999. Phase boundary propagation in a heterogeneous body. In: Proceedings: Mathematical, Physical and Engineering Sciences, pp. 757–766.

Bhattacharya, K., 2003. Microstructure of Martensite: Why it Forms and How it Gives Rise to the Shape-Memory Effect. Oxford University Press, Great Clarendon Street, Oxford, UK.

Blesgen, T., Fraternali, F., Raney, J.R., Amendola, A., Daraio, C., 2012. Continuum limits of bistable spring models of carbon nanotube arrays accounting for material damage. Mech. Res. Commun. 45, 58–63.

Bouaziz, O., Masse, J.P., Allain, S., Orgas, L., Latil, P., 2013. Compression of crumpled aluminum thin foils and comparison with other cellular materials. Mater. Sci. Eng. 570, 1–7.

BrielandShoultz, A., Tawfick, S., Park, S.J., Bedewy, M., Maschmann, M.R., Baur, J.W., Hart, A.J., 2014. Scaling the stiffness, strength, and toughness of ceramic coated nanotube foams into the structural regime. Adv. Funct. Mater. 24 (36), 5728–5735.

Cao, A., Dickrell, P.L., Sawyer, W.G., Ghasemi-Nejhad, M.N., Ajayan, P.M., 2005. Super-compressible foamlike carbon nanotube films. Science 310 (5752), 1307–1310.

Choong, L.T., Mannarino, M.M., Basu, S., Rutledge, G.C., 2013. Compressibility of electrospun fiber mats. J. Mater. Sci. 48 (22), 7827–7836.

Coleman, J.N., Khan, U., Blau, W.J., Gunko, Y.K., 2006. Small but strong: a review of the mechanical properties of carbon nanotube polymer composites. Carbon N Y 44 (9), 1624–1652.

Craig, R.F., 2013. Soil Mechanics. Springer, New York.

Davami, K., Jiang, Y., Cortes, J., Lin, C., Shaygan, M., Turner, K.T., Bargatin, I., 2016. Tuning the mechanical properties of vertical graphene sheets through atomic layer deposition. Nanotechnology 27 (15), 155701.

Eberl, C., Thompson, R., Gianola, D., Sharpe, W. J., Hemker, K., 2006. Digital image correlation and tracking. MatLabCentral, Mathworks file Exch. server, FileID, 12413, URL: https://www.mathworks.com/matlabcentral/fileexchange/.

Fan, S., Chapline, M.G., Franklin, N.R., Tombler, T.W., Cassell, A.M., Dai, H., 1999. Self-oriented regular arrays of carbon nanotubes and their field emission properties. Science 283 (5401), 512–514.

Fraternali, F., Blesgen, T., Amendola, A., Daraio, C., 2011. Multiscale mass-spring models of carbon nanotube foams. J. Mech. Phys. Solids 59 (1), 89–102.

Gibson, L.J., Ashby, M.F., 1999. Cellular Solids: Structure and Properties. Cambridge university press, New York.

Gong, L., Kyriakides, S., Jang, W.Y., 2005. Compressive response of open-cell foams. part i: morphology and elastic properties. Int. J. Solids Struct. 42 (5), 1355–1379.

Halonen, N., Rautio, A., Leino, A.R., Kyllonen, T., Toth, G., Lappalainen, J., Szabo, M., 2010. Three-dimensional carbon nanotube scaffolds as particulate filters and catalyst support membranes. ACS Nano 4 (4), 2003–2008.

Hata, K., Futaba, D.N., Mizuno, K., Namai, T., Yumura, M., Iijima, S., 2004. Water-assisted highly efficient synthesis of impurity-free single-walled carbon nanotubes. Science 306 (5700), 1362–1364.

Hutchens, S.B., Hall, L.J., Greer, J.R., 2010. In situ mechanical testing reveals periodic buckle nucleation and propagation in carbon nanotube bundles. Adv. Funct. Mater. 20 (14), 2338–2346.

Hutchens, S.B., Needleman, A., Greer, J.R., 2011. Analysis of uniaxial compression of vertically aligned carbon nanotubes. J. Mech. Phys. Solids 59 (10), 2227–2237.

Hutchens, S.B., Needleman, A., Greer, J.R., 2012. A microstructurally motivated description of the deformation of vertically aligned carbon nanotube structures. Appl. Phys. Lett. 100 (12), 121910.

Israelachvili, J.N., 2011. Intermolecular and Surface Forces. Academic press, Cambridge, MA.

Johnson, K.L., 1985. Contact Mechanics. Cambridge University Press, New York.

Kim, O.V., Liang, X., Litvinov, R.I., Weisel, J.W., Alber, M.S., Purohit, P.K., 2015. Foam–like compression behavior of fibrin networks. Biomech. Model. Mechanobiol. 1–16.

Koiter, W.T., 1964. On the dynamic boundary conditions in the theory of thin shells. In: Proc. Konikl. Ned. Acad. Wetenscap, pp. 117–126.

Komori, T., Itoh, M., 1994. A modified theory of fiber contact in general fiber assemblies. Text. Res. J. 64 (9), 519–528.

Lakes, R., Rosakis, P., Ruina, A., 1993. Microbuckling instability in elastomeric cellular solids. J. Mater. Sci. 28 (17), 4667–4672.

Lee, D.H., Carnaby, G.A., Tandon, S.K., 1992. Compressional energy of the random fiber assembly part ii: evaluation. Text. Res. J. 62 (5), 258–265.

Li, H., Lu, W.G., Li, J.J., Bai, X.D., Gu, C.Z., 2005. Multichannel ballistic transport in multiwall carbon nanotubes. Phys. Rev. Lett. 95 (8), 086601.

Magagnosc, D.J., Ehrbar, R., Kumar, G., He, M.R., Schroers, J., Gianola, D.S., 2013. Tunable tensile ductility in metallic glasses. Sci. Rep. 3.

Maschmann, M.R., Ehlert, G.J., Park, S.J., Mollenhauer, D., Maruyama, B., Hart, A.J., Baur, J.W., 2012. Visualizing strain evolution and coordinated buckling within CNT arrays by in situ digital image correlation. Adv. Funct. Mater. 22 (22), 4686–4695.

Masse, J.P., Poquillon, D., 2013. Mechanical behavior of entangled materials with or without cross-linked fibers. Scr. Mater. 68 (1), 39–43.

McCarter, C.M., Richards, R.F., Mesarovic, S.D., Richards, C.D., Bahr, D.F., McClain, D., Jiao, J., 2006. Mechanical compliance of photolithographically defined vertically aligned carbon nanotube turf. J. Mater. Sci. 41 (23), 7872–7878.

Meaud, J., Sain, T., Yeom, B., Park, S.J., Shoultz, A.B., Hulbert, G., Waas, A.M., 2014. Simultaneously high stiffness and damping in nanoengineered microtruss composites. ACS Nano 8 (4), 3468–3475.

Mesarovic, S.D., McCarter, C.M., Bahr, D.F., Radhakrishnan, H., Richards, R.F., Richards, C.D., Jiao, J., 2007. Mechanical behavior of a carbon nanotube turf. Scr. Mater. 56 (2), 157–160.

Mezeix, L., Bouvet, C., Huez, J., Poquillon, D., 2009. Mechanical behavior of entangled fibers and entangled cross-linked fibers during compression. J. Mater. Sci. 44 (14), 3652–3661.

Mindlin, R.D., Eshel, N.N., 1968. On first strain-gradient theories in linear elasticity. Int. J. Solids Struct. 4 (1), 109–124.

Onck, P.R., Koeman, T., Van Dillen, T., Van der Giessen, E., 2005. Alternative explanation of stiffening in cross-linked semiflexible networks. Phys. Rev. Lett. 95 (17), 178102.

Park, S.J., Schmidt, A.J., Bedewy, M., Hart, A.J., 2013a. Measurement of carbon nanotube microstructure relative density by optical attenuation and observation of size-dependent variations. Phys. Chem. Chem. Phys. 15 (27), 11511–11519.

Park, S.J., Schmidt, A.J., Bedewy, M., Hart, A.J., 2013b. Measurement of carbon nanotube microstructure relative density by optical attenuation and observation of size-dependent variations. Phys. Chem. Chem. Phys. 15 (27), 11511–11519.

Pathak, S., Lim, E.J., Saeed, PourShahid, Abadi, P., Graham, S., Cola, B.A., Greer, J.R., 2012. Higher recovery and better energy dissipation at faster strain rates in carbon nanotube bundles: an in-situ study. ACS Nano 6 (3), 2189–2197.

Peng, B., Locascio, M., Zapol, P., Li, S., Mielke, S.L., Schatz, G.C., Espinosa, H.D., 2008. Measurements of near-ultimate strength for multiwalled carbon nanotubes and irradiation-induced crosslinking improvements. Nat Nanotechnol 3 (10), 626–631.

Purohit, P.K., 2001. Dynamics of phase transitions in strings, beams and atomic chains. California Institute of Technology Ph.d thesis.

Qiu, A., Bahr, D.F., 2013. The role of density in the mechanical response of CNT turfs. Carbon N Y 55, 335–342.

Qiu, A., Bahr, D.F., Zbib, A.A., et al., 2011. Local and non-local behavior and coordinated buckling of CNT turfs. Carbon N Y 49, 1430–1438.

Radhakrishnan, H., Mesarovic, S.D., Qiu, A., Bahr, D.F., 2013. Phenomenological constitutive model for a CNT turf. Int. J. Solids Struct. 50 (14), 2224–2230.

Raney, J.R., Fraternali, F., Daraio, C., 2013a. Rate-independent dissipation and loading direction effects in compressed carbon nanotube arrays. Nanotechnology 24 (25), 255707.

Raney, J.R., Wang, R.Y., Daraio, C., 2013b. Control of microstructural heterogeneities in carbon nanotube foams. Carbon N Y 52, 193–200.

Taphouse, J.H., Smith, O.N.L., Marder, S.R., Cola, B.A., 2014. A pyrenylpropyl phosphonic acid surface modifier for mitigating the thermal resistance of carbon nanotube contacts. Adv. Funct. Mater. 24 (4), 465–471.

Tawfick, S., O'brien, K., Hart, A.J., 2009. Flexible high conductivity carbon nanotube interconnects made by rolling and printing. Small 5 (21), 2467–2473.

Thevamaran, R., Meshot, E.R., Daraio, C., 2015. Shock formation and rate effects in impacted carbon nanotube foams. Carbon N Y 84, 390–398.

Toll, S., 1998. Packing mechanics of fiber reinforcements. Polym. Eng. Sci. 38 (8), 1337–1350.

Torabi, H., Radhakrishnan, H., Mesarovic, S.D., 2014. Micromechanics of collective buckling in CNT turfs. J. Mech. Phys. Solids 72, 144–160.
Toupin, R.A., 1962. Elastic materials with couple-stresses. Arch. Ration. Mech. Anal. 11 (1), 385–414.
Treacy, M.J., Ebbesen, T.W., Gibson, J.M., 1996. Exceptionally high young's modulus observed for individual carbon nanotubes. Nature 381 (6584), 678–680.
Truskinovsky, L., Vainchtein, A., 2005. Kinetics of martensitic phase transitions: lattice model. SIAM J. Appl. Math. 66 (2), 533–553.
Turtletaub, S., 1997. Viscosity and strain gradient effects in the kinetics of propagating phase boundaries in solids. J. Elast. 46, 53–90.
Van Wyk, C.M., 1946. Note on the compressibility of wool. Journal of the Textile Institute Transactions 37 (12), T285–T292.
Volkov, A., Simiov, K., Zhigilei, L., 2009. Mesoscopic simulation of self-assembly of carbon nanotubes into a network of bundles. In: Proc. 47th AIAA Aerospace Sciences Meeting, p. 1544.
Yoffe, E.H., 1984. Modified hertz theory for spherical indentation. Philos. Mag. A 50 (6), 813–828.
Yu, C., Shi, L., Yao, Z., Li, D., Majumdar, A., 2005. Thermal conductance and thermopower of an individual single-wall carbon nanotube. Nano Lett. 5 (9), 1842–1846.
Zbib, A.A., Mesarovic, S.D., Lilleodden, E.T., McClain, D., Jiao, J., Bahr, D.F., 2008. The coordinated buckling of carbon nanotube turfs under uniform compression. Nanotechnology 19 (17), 175704.
Zhao, Q., Purohit, P.K., 2014. Extracting a kinetic relation from the dynamics of a bistable chain. Modell. Simul. Mater. Sci. Eng. 22 (4), 045004.
Zhao, Q., Purohit, P.K., 2016. (Adiabatic) phase boundaries in a bistable chain with twist and stretch. J. Mech. Phys. Solids 92, 176–194.
Zhao, X., Strickland, D.J., Derlet, P.M., He, M.R., Cheng, Y.J., Pu, J., Gianola, D.S., 2015. In situ measurements of a homogeneous to heterogeneous transition in the plastic response of ion-irradiated < 111 > ni microspecimens. Acta Mater. 88, 121–135.